Materials Science & Engineering A 874 (2023) 145073

Contents lists available at ScienceDirect

Materials Science & Engineering A

journal homepage: www.elsevier.com/locate/msea

Tuning the grain and domain sizes to achieve superior room-temperature tensile ductility in a B2-ordered refractory $Al_{15}Nb_{40}Ti_{40}V_5$ medium-entropy alloy

N. Yurchenko [a,b,*], E. Panina [a], A. Tojibaev [a], V. Novikov [a], G. Salishchev [a], S. Zherebtsov [a,b], N. Stepanov [a,b]

[a] Belgorod National Research University, Belgorod, 308015, Russia
[b] World-Class Research Center "Advanced Digital Technologies", State Marine Technical University, Saint Petersburg, 198095, Russia

ARTICLE INFO

Keywords:
Refractory high/medium-entropy alloys
B2 structure
Hall-Petch relation
Mechanical properties
Plastic deformation

ABSTRACT

Herein, we showed that the grain size, rather than the domain size, controlled room-temperature properties of a B2-ordered refractory $Al_{15}Nb_{40}Ti_{40}V_5$ medium-entropy alloy. Grain refinement to 20 μm at any size of B2 domains resulted in elongation of ~50%, which was superior to all the reported refractory high/medium-entropy alloys.

1. Introduction

Refractory high/medium-entropy alloys (RH/MEAs) are of great interest for the researchers worldwide due to their capacity to withstand extreme loads and oxidation at temperatures exceeding the operation limit of Ni-based superalloys [1–7]. However, most of RH/MEAs suffer from brittleness at ambient-to-medium temperatures under tension [8,9] or even compression [2,10–13] that hinders their industrial-scale structural applications. Until 2014, only one inherently ductile RHEA, namely, an equiatomic HfNbTaTiZr alloy with a body-centred cubic (bcc) structure [14–16], was discovered. The HfNbTaTiZr alloy could be processed by a simple routine including cold rolling and subsequent annealing [17]. Applying such thermomechanical treatment, Juan et al. [18] refined the grain size of this alloy and simultaneously improved its strength and ductility. Although the grain boundary strengthening in the HfNbTaTiZr RHEA was less effective than that of face-centred cubic (fcc) H/MEAs and austenitic steels [19], it remained an attractive way to achieve advanced and, most importantly, balanced mechanical performance compared to the secondary phase hardening [20] leading to reduced ductility [21].

Since 2014, many ductile RH/MEAs have been reported [22–45], and, among them, Al-containing alloys attracted particular attention [23,29,35,37–40,44,45], as some of the latter demonstrated better mechanical properties compared to Al-free counterparts owing to a B2 (ordered bcc) structure that appeared in a form of B2 domains [37–39,44,45]. Meantime, most of the data are still presented for either unprocessed, as-cast state, or for the processed state with a certain grain size, thus making the estimation of grain boundary strengthening unreliable. In the case of B2 domains, which size can range from <1 nm to tens and hundreds of nanometers depending on the chemical composition [37–39,44,45], it is also unclear how this parameter affects the strength and ductility, especially considering scarce experimental data on intermetallic alloys that suggest that the lower size of ordered domains led to the higher strength [46–48]. Thus, it seems highly important to evaluate the effect of both grain and domain sizes on the mechanical properties of these Al-containing B2-ordered RH/MEAs more systematically.

To address this issue, we comprehensively investigated the room-temperature tensile behaviour of recently introduced $Al_{15}Nb_{40}Ti_{40}V_5$ (at.%) RMEA with a weakly B2-ordered structure [39], in which both grain and B2 domain sizes could be tailored separately by varying processing (annealing treatment) conditions.

2. Materials and methods

The alloy with a nominal composition of $Al_{15}Nb_{40}Ti_{40}V_5$ was produced by vacuum arc melting of pure (>99.9 wt%) metals; the actual composition of the alloy is presented in Table S1, Supplementary

* Corresponding author. Belgorod National Research University, Belgorod 308015, Russia.
E-mail address: yurchenko_nikita@bsu.edu.ru (N. Yurchenko).

https://doi.org/10.1016/j.msea.2023.145073
Received 22 February 2023; Received in revised form 19 April 2023; Accepted 20 April 2023
Available online 21 April 2023

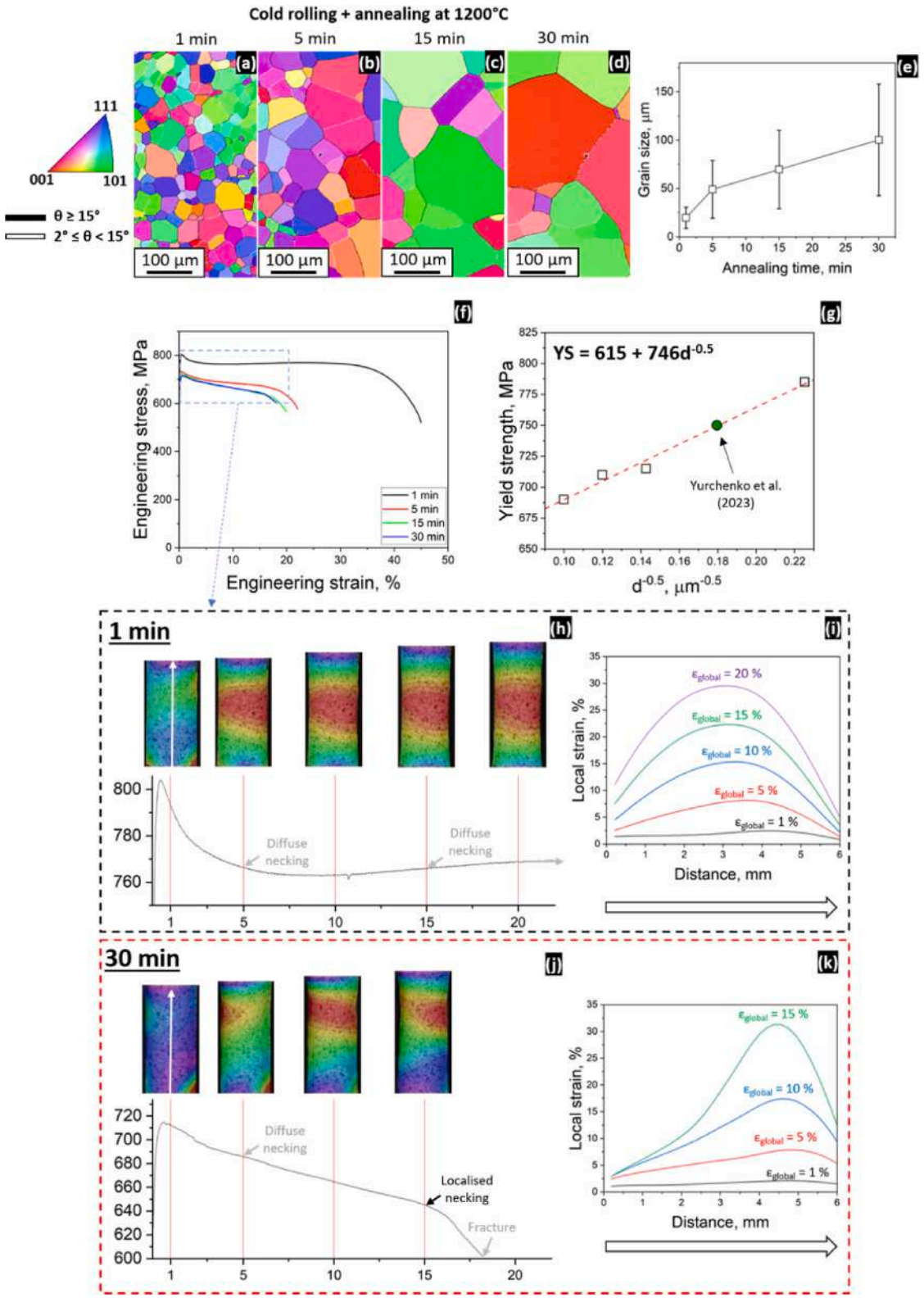

Fig. 1. Characterisation of the $Al_{15}Nb_{40}Ti_{40}V_5$ alloy annealed at 1200 °C for 1–30 min: (a–d) – Inverse Pole Figure (IPF) maps, showing typical microstructures after annealing; (e) – dependence of grain size on annealing time; (f) – engineering stress–strain curves obtained during room-temperature tensile tests; (g) – dependence of yield strength on the inverse square root of grain size, including data from Ref. [39], with the resulted Hall-Petch relation obtained by linear fitting; (h) – enlarged part of the stress–strain curve of the small-grained specimen and DIC snapshots of gauge section, corresponded to certain values of the global strain, ε_{global}; (i) – local strain distribution in the small-grained specimen along the gauge length (denoted with white arrow in the first DIC snapshot (h)) at corresponding values of the ε_{global}; (j) – enlarged part of the stress–strain curve of the coarse-grained specimen supplied by DIC snapshots of gauge section, corresponded to certain values of the ε_{global}; (k) – local strain distribution in the coarse-grained specimen along the gauge length (denoted with white arrow in the first DIC snapshot (j)) at corresponding values of the ε_{global}.

Table 1
Yield strength, *YS*, ultimate tensile strength, *UTS*, and elongation at fracture, *EF*, obtained during room-temperature tensile tests of the $Al_{15}Nb_{40}Ti_{40}V_5$ alloy annealed at 1200 °C for 1–30 min.

Annealing at 1200 °C	*YS*, MPa	*UTS*, MPa	*EF*, %
1 min	785 ± 15	805 ± 10	45.0 ± 1.8
5 min	715 ± 5	735 ± 5	22.0 ± 1.5
15 min	710 ± 5	720 ± 10	20.0 ± 0.8
30 min	690 ± 5	715 ± 10	18.2 ± 1.4

material. The as-cast ingot was subjected to a thermomechanical treatment including cold rolling to 80% of thickness and subsequent annealing in a Nabertherm furnace at 1200 °C for 1, 5, 15, and 30 min followed by water quenching. Some specimens annealed at 1200 °C for 1 min were further annealed at 800 °C for 5, 15, and 30 min followed by water quenching. Prior to annealing, the specimens were sealed in vacuumed (10^{-2} torr) tubes filled with titanium chips to prevent any oxidation.

Tensile tests of dog-bone specimens with the gauge dimensions of 6 × 3 × 1 mm^3 were performed at room-temperature at a constant strain rate of 10^{-3} s^{-1} using an Instron 5882 machine. The digital image correlation (DIC) technique was employed to visualise the distribution of local strains produced during the tensile tests. The in-plane Lagrangian strains were measured using a commercial Vic-3D™ system (Correlated Solutions, Inc) [37,39].

Microstructural investigations were performed using electron backscatter diffraction (EBSD; FEI Quanta 600 FEG) and transmission electron microscopy (TEM; JEM JEOL-2100). The average grain or B2 domain sizes were estimated using the linear intercept method [49].

3. Results and discussion

3.1. Effect of grain size

Fig. 1 collects data on the microstructure and corresponding mechanical properties of the $Al_{15}Nb_{40}Ti_{40}V_5$ RMEA annealed at 1200 °C for 1–30 min. According to EBSD analysis, annealing led to the formation of fully recrystallised microstructures (Fig. 1(a–d)), which average grain sizes increased with the annealing time from ~20 μm after 1 min to ~ 100 μm after 30 min (Fig. 1(e)). TEM studies revealed close sizes of B2 domains (~40 nm; Fig. S1, Supplementary material) and no secondary phase particles, while gas fusion analysis showed comparative levels of contamination (Table S2, Supplementary material) for each annealing time, thereby excluding other (than grain size) factors which could affect the mechanical properties.

Fig. 1(f) demonstrates engineering tensile stress-strain curves of the specimens with different grain sizes; Table 1 summarises yield strength, *YS*, ultimate strength, *UTS*, and elongation at fracture, *EF*, obtained during the tests. The small-grained specimen (referred to as 1 min in Fig. 1(f)) showed the highest *YS*, *UTS*, and *EF*. The grain growth up to 50 μm (5 min) led to a steep degradation of mechanical properties, especially ductility. The *EF* value of the 50 μm–specimen was twice lower than that of the 20 μm–specimen. Meantime, the further grain growth up to 70–100 μm (15–30 min) resulted in more gradual softening and ductility reduction (Fig. 1(f), Table 1).

The dependence between the *YS* and grain sizes, including our previous data [39], was found (Fig. 1(g)) to be properly described by a linear function and agreed with the well-known Hall-Petch relation [50]:

$$\sigma_{YS} = \sigma_0 + k_y d^{-\frac{1}{2}} \quad (1)$$

where σ_0 is a friction stress, k_y is the Hall-Petch coefficient, and d is the grain size. We found that $\sigma_0 = 615$ MPa and $k_y = 746$ MPa $\mu m^{-1/2}$. The k_y value determined for the $Al_{15}Nb_{40}Ti_{40}V_5$ RMEA was ~3 times higher than that of the HfNbTaTiZr RHEA [18,19], indicating a more pronounced grain boundary strengthening in the alloy studied. Still, this value was smaller compared to some other RH/MEAs [51–53].

The alteration of post-yielding behaviour with an increase in the grain size should also be noted. In all the specimens, we observed a short strain-hardening stage before attaining the *UTS* then followed by a pronounced softening stage (Fig. 1(f)). But, if, in the small-grained specimen, this softening reached an inflection point, after which slight strain hardening was recovered, in the specimens with the larger grain sizes, the softening stage was continuous, leading to a much faster failure.

To get a better perception of such distinct behaviours, we applied the DIC method during testing (Fig. 1(h–k)). Snapshots of the gauge sections taken at certain global strains, ε_{global}, showed that the plastic deformation was non-uniform in the specimens both with the smallest (20 μm; 1 min) and the largest (100 μm; 30 min) grain sizes; however, the level of this localisation differed notably. Independently on the grain size, the plastic deformation up to $\varepsilon_{global} = 5\%$ was accompanied by the formation of diffuse necking, as seen from both DIC snapshots and the local strain distributions. Meantime, with the further increase in the ε_{global} up to 15%, the local strain distribution indicated that the diffuse necking still preserved in the 20 μm-specimen, yet, in the 100 μm–specimen, it evolved into localised necking, judging from the sharpening of the local strain distribution (Fig. 1(h–k)).

Apparently, such a difference in the deformation behaviour could stem from the distinct microstructural response to straining. We have examined the near-fracture regions of the tensile specimens with various grain sizes (Fig. 2). EBSD analysis showed that the 20 μm–specimen was deformed more homogeneously compared to the specimens with larger grain sizes. Similar to conventional alloys [54–56], Kernel Average Misorientation (KAM) maps (Fig. 2) revealed that the small-grained specimen contained high density of geometrically necessary dislocations (GNDs) within the grain interiors, while, in the coarse-grained specimens, GNDs accumulated near the grain boundaries mainly. The higher density of GNDs and their more homogeneous distribution in the small-grained specimen indicated better compatibility and coordination of plastic deformation without severe localisation at both micro- and macro-level (localised necking) [56]. Meanwhile, the coarse-grained specimens with GNDs located nearby the grain boundaries had lesser possibilities to accommodate strains that arose during the tensile load resulting in a faster formation of localised necking followed by a premature fracture [56].

3.2. Effect of B2 domain size

For the small-grained state, which showed the best mechanical properties, we also evaluated the effect of B2 domain size. To manipulate the latter parameter, we additionally annealed the specimens at 800 °C for various times. Before annealing (this state is denoted as 0 min hereafter), the grain interiors consisted of profuse B2 domains (white entities) with a size of ~40 nm separated by antiphase domain boundaries (APDBs; dark interlayers) (Fig. 3(a)). After annealing at 800 °C for 5, 15, and 30 min, B2 domains grew up to ~105, 210, and 430 nm, respectively (Fig. 3(b–e)). The existing data suggest that the coarsening of B2 domains could occur without the alternating degree of order [57]. Besides, no secondary phases, grain growth (Fig. S2, Supplementary material), or changes in the contamination level (Table S3, Supplementary material) were detected, thus omitting other (than B2 domain size) factors that could impact the mechanical performance.

Unlike the grain size, the variations in the B2 domain sizes had almost no effect on the mechanical properties (Fig. 3(f), Table 2). At all the B2 domain sizes, we found very close values of *YS*, *UTS*, and *EF*; however, small deviations of *EF* should be noted. We did not find any correlation between the *YS* and B2 domain sizes (Fig. 3(g)). No significant difference in the post-yielding behaviour was also revealed. Similar to the specimens with the smallest B2 domains (Fig. 3(h)), the stress-strain curves of the specimens with the largest B2 domains contained

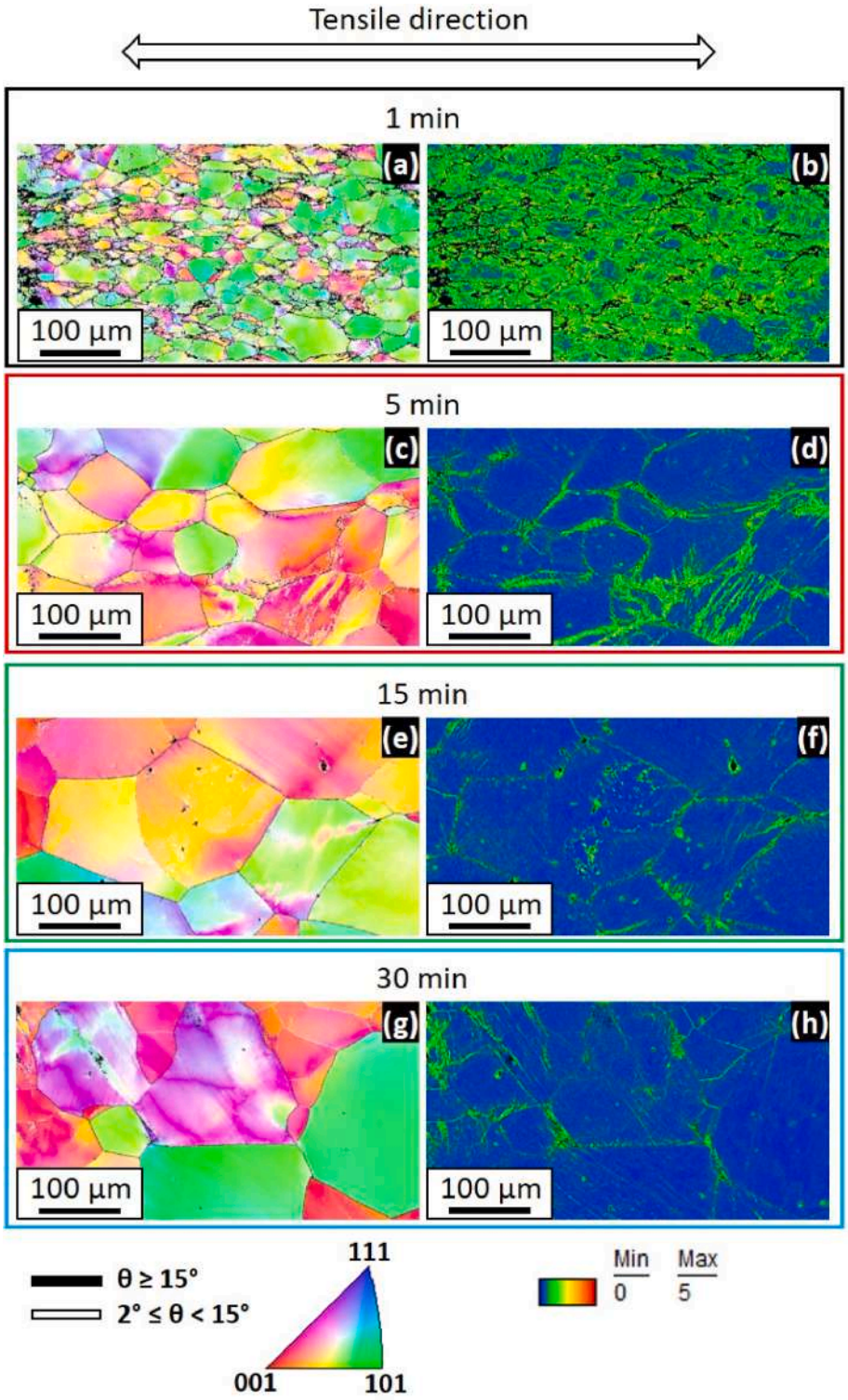

Fig. 2. Characterisation of the near-fracture regions of tensile specimens of the $Al_{15}Nb_{40}Ti_{40}V_5$ alloy annealed at 1200 °C for 1 (a, b), 5 (c, d), 15 (e, f), and 30 (g, h) min: (a, c, e, g) – IPF maps; (b, d, f, h) – KAM maps.

a short strain hardening stage followed by an exponential-like decay of the flow stress with the formation of the diffuse necking, and then reaching the inflection point at the ε_{global} = 10%, after which minor strengthening stage reappeared (Fig. 3(j)). According to the local strain distribution, the diffuse necking persisted in the specimens with the large B2 domains even after achieving the ε_{global} = 15% (Fig. 3(i, k)), a critical value for the localised necking in the coarse-grained specimens.

Scarce experimental data reported that the size of ordered domains, which was controlled by isothermal annealing, could affect mechanical properties in such a fashion that their coarsening led to a lower strength [46–48]. Contrarily, we found that the B2 domain size, at a constant degree of order, had no notable influence on the strength-ductility synergy and deformation behaviour. The detailed TEM studies showed almost no difference in the spatial distribution of dislocations in the

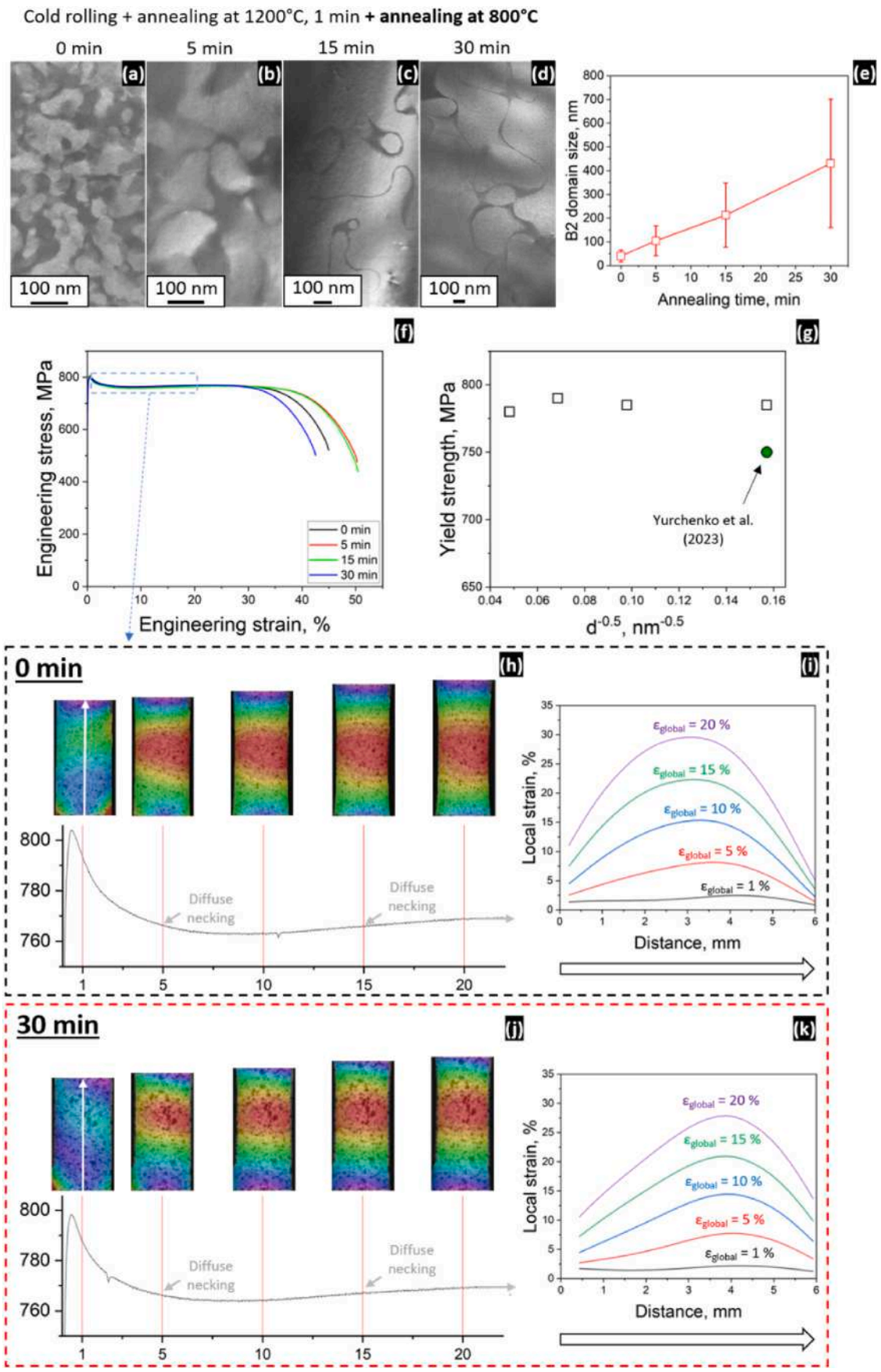

(caption on next page)

Fig. 3. Characterisation of the $Al_{15}Nb_{40}Ti_{40}V_5$ alloy after annealing at 1200 °C for 1 min and additional annealing at 800 °C for 0–30 min: (a–d) – dark-field TEM images taken at {100} superlattice spots in a <001/011> zone axis, showing a typical fine structure within the grain interiors, consisted of the B2 domains (white entities) and APDBs (dark interlayers); (e) – dependence of the B2 domain size on annealing time; (f) – engineering stress–strain curves obtained during room-temperature tensile tests; (g) – dependence of yield strength on the inverse square root of the B2 domain size, including data from Ref. [39]; (h) – enlarged part of the stress–strain curve of the specimen with the smallest B2 domains supplied by DIC snapshots of gauge section, corresponded to certain values of the ε_{global}; (i) – local strain distribution in the specimen with the smallest B2 domains along the gauge length (denoted with white arrow in the first DIC snapshot (h)) at the corresponding values of the ε_{global}; (j) – enlarged part of the stress–strain curve of the specimen with the largest B2 domains supplied by DIC snapshots of gauge section, corresponded to certain values of the ε_{global}; (k) – local strain distribution in the specimen with the largest B2 domains along the gauge length (denoted with white arrow in the first DIC snapshot (j)) at corresponding values of the ε_{global}.

Table 2
Yield strength, *YS*, ultimate tensile strength, *UTS*, and elongation at fracture, *EF*, obtained during room-temperature tensile tests of the $Al_{15}Nb_{40}Ti_{40}V_5$ alloy after annealing at 1200 °C for 1 min and additional annealing at 800 °C for 0–30 min.

Annealing at 1200 °C, 1 min + annealing at 800 °C	*YS*, MPa	*UTS*, MPa	*EF*, %
0 min	785 ± 15	805 ± 10	45.0 ± 1.8
5 min	785 ± 5	800 ± 5	50.3 ± 3.2
15 min	790 ± 10	800 ± 5	50.4 ± 4.6
30 min	780 ± 15	800 ± 10	42.5 ± 2.9

specimens with small and large B2 domains (Fig. 4). Independently on the B2 domain sizes, the dislocation motion was confined within intersected dislocation bands, and no pinning of dislocations by B2 domains was found, compared to intermediate temperature [39].

The degree of interaction of dislocations with the B2 domains should depend on the antiphase boundary (APB) energy [58]. Several studies showed that, in ternary B2-ordered Nb-rich alloys [59,60], the APB energy was rather low thus allowing relatively easy glide of dislocations albeit within narrow bands. In the case of the $Al_{15}Nb_{40}Ti_{40}V_5$ alloy, the results obtained also suggest the modest APB energy (however, the estimation of the exact APB energy value requires an additional in-depth study) that could reasonably explain an insensitivity of the mechanical properties to the variations in the B2 domain sizes in terms of the weak interactions of dislocations with these entities [61].

3.3. Comparison of mechanical properties

Grain refinement of the $Al_{15}Nb_{40}Ti_{40}V_5$ alloy to ~20 μm at any size of B2 domains resulted in the best properties, namely *YS* ≈ 780–790 MPa and *EF* ≈ 50%. We compared these values with other RH/MEAs. For that, we collected dataset of room-temperature tensile properties for different RH/MEAs both in the as-cast and processed states (see Table S4, Supplementary material; the dataset contains more than 140 entities), and grouped them as follows: (i) RH/MEAs comprised of mostly refractory metals (RH/MEAs in Fig. 5), (ii) Al-containing RH/MEAs (Al-RH/MEAs), (iii) RH/MEAs manifested transformation-induced plasticity (TRIP) effect (TRIP RH/MEAs), and (iv) interstitial-containing RH/MEAs (i-RH/MEAs).

Within the dataset, a typical strength-ductility dilemma could be

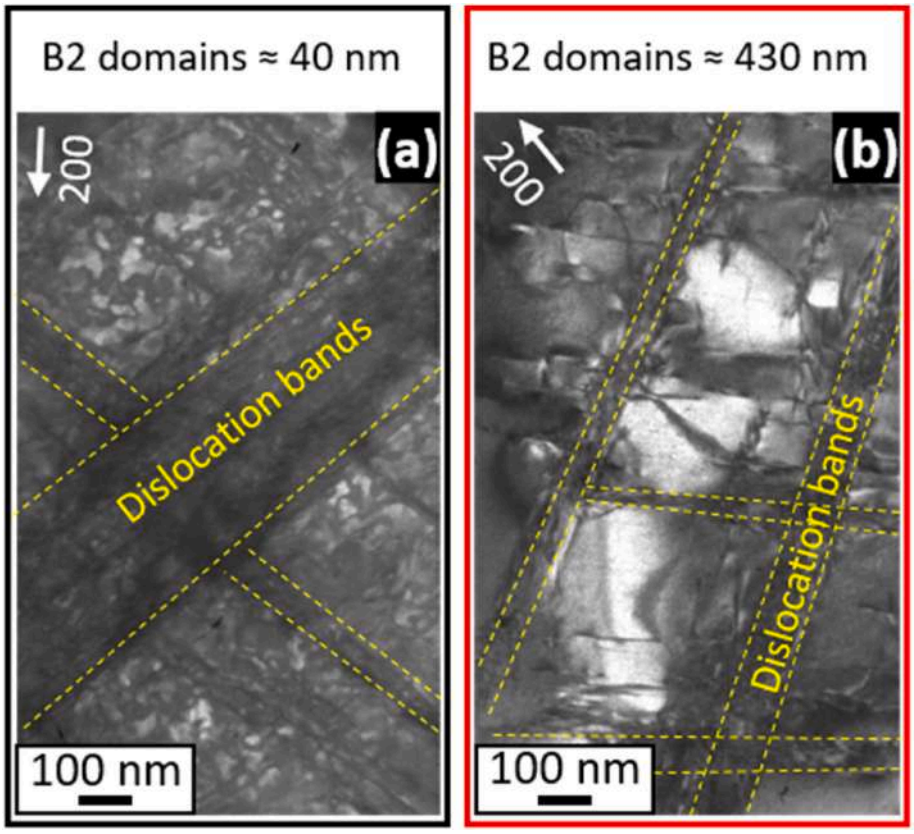

Fig. 4. Dark-field TEM images of typical dislocation structures of the $Al_{15}Nb_{40}Ti_{40}V_5$ alloy with the smallest (a) and largest (b) B2 domain sizes. Dashed yellow lines denote the dislocation bands. (For interpretation of the references to colour in this figure legend, the reader is referred to the Web version of this article.)

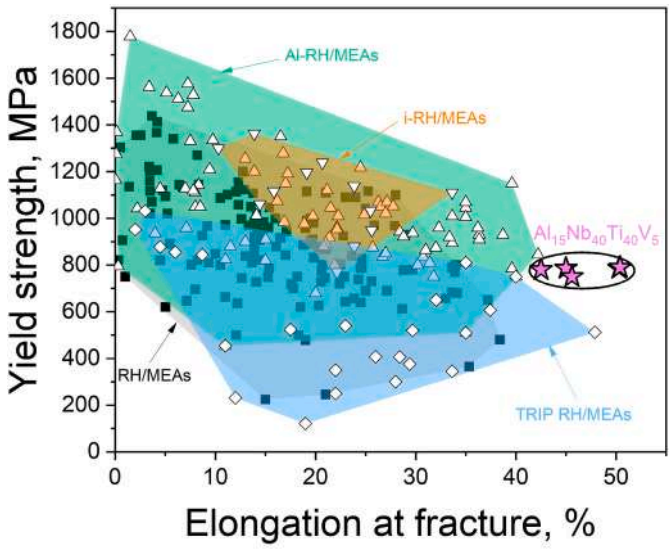

Fig. 5. Comparison of the tensile yield strength and elongation at fracture values of the small-grained $Al_{15}Nb_{40}Ti_{40}V_5$ alloy with different groups of RH/MEAs available in literature, including RH/MEAs, Al-RH/MEAs, i-RH/MEAs, and TRIP RH/MEAs. Data used for comparison are summarised in Table S4, Supplementary material.

revealed: the *YS* decreased with an increase in the *EF*. The highest *YS* values were observed in Al-RH/MEAs, while TRIP RH/MEAs demonstrated the lowest strength, and, in-between, RH/MEAs and i-RH/MEAs were positioned. In turn, none of the previously reported RH/MEAs could achieve the 50 %-elongation. The former most ductile ($EF \approx 48\%$) $Ti_{50}Zr_{30}Hf_{10}Nb_{10}$ TRIP RMEA had the $YS = 512$ MPa [62]. The $Al_{15}Nb_{40}Ti_{40}V_5$ alloy appeared to be even more ductile and ~35 %-stronger. The superior combination of mechanical properties in the small-grained $Al_{15}Nb_{40}Ti_{40}V_5$ alloy confirms the efficiency of grain refinement as an alternative way to conquer strength-ductility trade-off in RH/MEAs [18,19,24,37].

4. Conclusions

For the first time, the effect of grain and domain sizes on the room-temperature tensile behaviour of B2-ordered RH/MEAs was systematically studied. For a model B2-ordered $Al_{15}Nb_{40}Ti_{40}V_5$ RMEA, we showed that the mechanical properties were highly dependent on the grain size and insensitive to the B2 domain sizes. Grain boundary strengthening in this alloy was found to be ~3 times more efficient than in a well-known bcc HfNbTaTiZr RHEA. Independently on the B2 domain size, the smallest grains of ~20 μm ensured the most stable plastic flow without the premature formation of the localised necking, thereby achieving the elongation of ~50%, which was superior to all the RH/MEAs reported to date.

Originality statement

I write on behalf of myself and all co-authors to confirm that the results reported in the manuscript are original and neither the entire work, nor any of its parts have been previously published. The authors confirm that the article has not been submitted to peer review, nor has been accepted for publishing in another journal. The author(s) confirms that the research in their work is original, and that all the data given in the article are real and authentic. If necessary, the article can be recalled, and errors corrected.

CRediT authorship contribution statement

N. Yurchenko: Conceptualization, Validation, Formal analysis, Investigation, Data curation, Writing – original draft, Writing – review & editing, Visualization, Supervision, Project administration, Funding acquisition. **E. Panina:** Methodology, Investigation. **A. Tojibaev:** Methodology, Investigation. **V. Novikov:** Methodology, Investigation. **G. Salishchev:** Validation, Formal analysis, Data curation, Writing – review & editing, Supervision. **S. Zherebtsov:** Writing – review & editing, Supervision. **N. Stepanov:** Writing – review & editing, Supervision.

Declaration of competing interest

The authors declare that they have no known competing financial interests or personal relationships that could have appeared to influence the work reported in this paper.

Data availability

Data will be made available on request.

Acknowledgements

Funding: This work was supported by the Russian Science Foundation Grant no. 21-79-10043 (https://rscf.ru/en/project/21-79-10043/). A part of this research (gas fusion analysis) was partially funded by the Ministry of Science and Higher Education of the Russian Federation as part of the World-Class Research Center program: Advanced Digital Technologies (Contract no. N° 075-15-2022-312 dated April 20, 2022).

The work was carried out using the equipment of the Joint Research Center of Belgorod State National Research University « Technology and Materials». The authors also thank Dr S. Naumov, Belgorod National Research University, for aid in preparing the ingot of the alloy.

Appendix A. Supplementary data

Supplementary data to this article can be found online at https://doi.org/10.1016/j.msea.2023.145073.

References

[1] O.N. Senkov, G.B. Wilks, D.B. Miracle, C.P. Chuang, P.K. Liaw, Refractory high-entropy alloys, Intermetallics 18 (2010) 1758–1765, https://doi.org/10.1016/j.intermet.2010.05.014.

[2] O.N. Senkov, G.B. Wilks, J.M. Scott, D.B. Miracle, Mechanical properties of $Nb_{25}Mo_{25}Ta_{25}W_{25}$ and $V_{20}Nb_{20}Mo_{20}Ta_{20}W_{20}$ refractory high entropy alloys, Intermetallics 19 (2011) 698–706, https://doi.org/10.1016/j.intermet.2011.01.004.

[3] O.N. Senkov, D. Isheim, D.N. Seidman, A.L. Pilchak, Development of a refractory high entropy superalloy, Entropy 18 (2016) 1–13, https://doi.org/10.3390/e18030102.

[4] B. Gorr, F. Müller, S. Schellert, H.-J. Christ, H. Chen, A. Kauffmann, M. Heilmaier, A new strategy to intrinsically protect refractory metal based alloys at ultra high temperatures, Corrosion Sci. (2020), 108475, https://doi.org/10.1016/j.corsci.2020.108475.

[5] S. Wu, D. Qiao, H. Zhang, J. Miao, H. Zhao, J. Wang, Y. Lu, T. Wang, T. Li, Microstructure and mechanical properties of $C_xHf_{0.25}NbTaW_{0.5}$ refractory high-entropy alloys at room and high temperatures, J. Mater. Sci. Technol. 97 (2022) 229–238, https://doi.org/10.1016/J.JMST.2021.05.015.

[6] Q. Wei, X. Xu, Q. Shen, G. Luo, J. Zhang, J. Li, Q. Fang, C.-T. Liu, M. Chen, T.-G. Nieh, J. Chen, Metal-carbide eutectics with multiprincipal elements make superrefractory alloys, Sci. Adv. 8 (2022), https://doi.org/10.1126/SCIADV.ABO2068.

[7] Y. Zhang, Q. Wei, P. Xie, X. Xu, An ultrastrong niobium alloy enabled by refractory carbide and eutectic structure, Mater. Res. Lett. 11 (2022) 169–178, https://doi.org/10.1080/21663831.2022.2133977.

[8] P. Kumar, S.J. Kim, Q. Yu, J. Ell, M. Zhang, Y. Yang, J.Y. Kim, H.K. Park, A. M. Minor, E.S. Park, R.O. Ritchie, Compressive vs. tensile yield and fracture toughness behavior of a body-centered cubic refractory high-entropy superalloy Al0.5Nb1.25Ta1.25TiZr at temperatures from ambient to 1200°C, Acta Mater. 245 (2023), 118620, https://doi.org/10.1016/J.ACTAMAT.2022.118620.

[9] M. Wu, S. Wang, F. Xiao, G. Shen, Y. Tian, C. Yang, G. Zhu, D. Wang, D. Shu, B. Sun, Designing lightweight dual-phase refractory VNbTiSi-based eutectic high-entropy alloys for use at elevated temperatures, Mater. Sci. Eng. 842 (2022), 143112, https://doi.org/10.1016/J.MSEA.2022.143112.

[10] O.N. Senkov, C. Woodward, D.B. Miracle, Microstructure and properties of aluminum-containing refractory high-entropy alloys, Jom 66 (2014) 2030–2042, https://doi.org/10.1007/s11837-014-1066-0.

[11] N.D. Stepanov, N.Y. Yurchenko, D.V. Skibin, M.A. Tikhonovsky, G.A. Salishchev, Structure and mechanical properties of the $AlCr_xNbTiV$ (x = 0, 0.5, 1, 1.5) high entropy alloys, J. Alloys Compd. 652 (2015) 266–280, https://doi.org/10.1016/j.jallcom.2015.08.224.

[12] H. Chen, A. Kauffmann, B. Gorr, D. Schliephake, C. Seemüller, J.N. Wagner, H. J. Christ, M. Heilmaier, Microstructure and mechanical properties at elevated temperatures of a new Al-containing refractory high-entropy alloy Nb-Mo-Cr-Ti-Al, J. Alloys Compd. 661 (2016) 206–215, https://doi.org/10.1016/j.jallcom.2015.11.050.

[13] N.Y. Yurchenko, N.D. Stepanov, S.V. Zherebtsov, M.A. Tikhonovsky, G. A. Salishchev, Structure and mechanical properties of B2 ordered refractory $AlNbTiVZr_x$ (x = 0–1.5) high-entropy alloys, Mater. Sci. Eng. 704 (2017) 82–90, https://doi.org/10.1016/j.msea.2017.08.019.

[14] O.N. Senkov, J.M. Scott, S.V. Senkova, D.B. Miracle, C.F. Woodward, Microstructure and room temperature properties of a high-entropy TaNbHfZrTi alloy, J. Alloys Compd. 509 (2011) 6043–6048, https://doi.org/10.1016/j.jallcom.2011.02.171.

[15] O.N. Senkov, J.M. Scott, S.V. Senkova, F. Meisenkothen, D.B. Miracle, C. F. Woodward, Microstructure and elevated temperature properties of a refractory TaNbHfZrTi alloy, J. Mater. Sci. 47 (2012) 4062–4074, https://doi.org/10.1007/s10853-012-6260-2.

[16] O.N. Senkov, D.B. Miracle, K.J. Chaput, J.P. Couzinie, Development and exploration of refractory high entropy alloys - a review, J. Mater. Res. 33 (2018) 3092–3128, https://doi.org/10.1557/jmr.2018.153.

[17] O.N. Senkov, S.L. Semiatin, Microstructure and properties of a refractory high-entropy alloy after cold working, J. Alloys Compd. 649 (2015) 1110–1123, https://doi.org/10.1016/j.jallcom.2015.07.209.

[18] C.C. Juan, M.H. Tsai, C.W. Tsai, W.L. Hsu, C.M. Lin, S.K. Chen, S.J. Lin, J.W. Yeh, Simultaneously increasing the strength and ductility of a refractory high-entropy alloy via grain refining, Mater. Lett. 184 (2016) 200–203, https://doi.org/10.1016/j.matlet.2016.08.060.

[19] S. Chen, K.K. Tseng, Y. Tong, W. Li, C.W. Tsai, J.W. Yeh, P.K. Liaw, Grain growth and Hall-Petch relationship in a refractory HfNbTaZrTi high-entropy alloy, J. Alloys Compd. 795 (2019) 19–26, https://doi.org/10.1016/j.jallcom.2019.04.291.

[20] N.D. Stepanov, N.Yu Yurchenko, S.V. Zherebtsov, M.A. Tikhonovsky, G. A. Salishchev, Aging behavior of the HfNbTaTiZr high entropy alloy, Mater. Lett. 211 (2018) 87–90, https://doi.org/10.1016/j.matlet.2017.09.094.

[21] O.N. Senkov, A.L. Pilchak, S.L. Semiatin, Effect of cold deformation and annealing on the microstructure and tensile properties of a HfNbTaTiZr refractory high entropy alloy, Metall. Mater. Trans. 49 (2018) 2876–2892, https://doi.org/10.1007/s11661-018-4646-8.

[22] Y.D. Wu, Y.H. Cai, T. Wang, J.J. Si, J. Zhu, Y.D. Wang, X.D. Hui, A refractory Hf25Nb25Ti25Zr25 high-entropy alloy with excellent structural stability and tensile properties, Mater. Lett. 130 (2014) 277–280, https://doi.org/10.1016/j.matlet.2014.05.134.

[23] Y. Wu, J. Si, D. Lin, T. Wang, W.Y. Wang, Y. Wang, Z. Liu, X. Hui, Phase stability and mechanical properties of AlHfNbTiZr high-entropy alloys, Mater. Sci. Eng. 724 (2018) 249–259, https://doi.org/10.1016/J.MSEA.2018.03.071.

[24] Z. Lei, X. Liu, Y. Wu, H. Wang, S. Jiang, S. Wang, X. Hui, Y. Wu, B. Gault, P. Kontis, D. Raabe, L. Gu, Q. Zhang, H. Chen, H. Wang, J. Liu, K. An, Q. Zeng, T.-G. Nieh, Z. Lu, Enhanced strength and ductility in a high-entropy alloy via ordered oxygen complexes, Nature 563 (2018) 546–550, https://doi.org/10.1038/s41586-018-0685-y.

[25] S.P. Wang, E. Ma, J. Xu, New ternary equi-atomic refractory medium-entropy alloys with tensile ductility: hafnium versus titanium into NbTa-based solution, Intermetallics 107 (2019) 15–23, https://doi.org/10.1016/j.intermet.2019.01.004.

[26] C. Zhang, B.E. MacDonald, F. Guo, H. Wang, C. Zhu, X. Liu, Y. Kang, X. Xie, Y. Zhou, K.S. Vecchio, E.J. Lavernia, Cold-workable refractory complex concentrated alloys with tunable microstructure and good room-temperature tensile behavior, Scripta Mater. 188 (2020) 16–20, https://doi.org/10.1016/j.scriptamat.2020.07.006.

[27] S. Wei, S.J. Kim, J. Kang, Y. Zhang, Y. Zhang, T. Furuhara, E.S. Park, C.C. Tasan, Natural-mixing guided design of refractory high-entropy alloys with as-cast tensile ductility, Nat. Mater. 19 (2020) 1175–1181, https://doi.org/10.1038/s41563-020-0750-4, 2020 1911.

[28] Y. Chen, Z. Xu, M. Wang, Y. Li, C. Wu, Y. Yang, A single-phase $V_{0.5}Nb_{0.5}ZrTi$ refractory high-entropy alloy with outstanding tensile properties, Mater. Sci. Eng. 792 (2020), 139774, https://doi.org/10.1016/J.MSEA.2020.139774.

[29] J. Pang, H. Zhang, L. Zhang, Z. Zhu, H. Fu, H. Li, A. Wang, Z. Li, H. Zhang, Ductile $Ti_{1.5}ZrNbAl_{0.3}$ refractory high entropy alloy with high specific strength, Mater. Lett. 290 (2021), 129428, https://doi.org/10.1016/j.matlet.2021.129428.

[30] Z. Han, L. Meng, J. Yang, G. Liu, J. Yang, R. Wei, G. Zhang, Novel BCC VNbTa refractory multi-element alloys with superior tensile properties, Mater. Sci. Eng. 825 (2021), 141908, https://doi.org/10.1016/j.msea.2021.141908.

[31] M. Wu, S. Wang, F. Xiao, G. Zhu, C. Yang, D. Shu, B. Sun, Dislocation glide and mechanical twinning in a ductile VNbTi medium entropy alloy, J. Mater. Sci. Technol. 110 (2022) 210–215, https://doi.org/10.1016/J.JMST.2021.09.016.

[32] Z.Q. Xu, Z.L. Ma, Y. Tan, X.W. Cheng, Designing TiVNbTaSi refractory high-entropy alloys with ambient tensile ductility, Scripta Mater. 206 (2022), 114230, https://doi.org/10.1016/J.SCRIPTAMAT.2021.114230.

[33] Y. Jia, G. Wang, S. Wu, Y. Mu, Y. Yi, Y. Jia, P.K. Liaw, T. Zhang, C.-T. Liu, A lightweight refractory complex concentrated alloy with high strength and uniform ductility, Appl. Mater. Today 27 (2022), 101429, https://doi.org/10.1016/j.apmt.2022.101429.

[34] W. Li, K. Xiong, L. Yang, S. Zhang, J. He, Y. Wang, Y. Mao, An ambient ductile TiHfVNbTa refractory high-entropy alloy: cold rolling, mechanical properties, lattice distortion, and first-principles prediction, Mater. Sci. Eng. 856 (2022), 144046, https://doi.org/10.1016/J.MSEA.2022.144046.

[35] S. Zeng, Y. Zhou, H. Li, H. Zhang, H. Zhang, Z. Zhu, Microstructure and mechanical properties of lightweight $Ti_3Zr_{1.5}NbVAl_x$ (x = 0, 0.25, 0.5 and 0.75) refractory complex concentrated alloys, J. Mater. Sci. Technol. 130 (2022) 64–74, https://doi.org/10.1016/J.JMST.2022.05.005.

[36] W. Huang, J. Hou, X. Wang, J. Qiao, Y. Wu, Excellent room-temperature tensile ductility in as-cast $Ti_{37}V_{15}Nb_{22}Hf_{23}W_3$ refractory high entropy alloys, Intermetallics 151 (2022), 107735, https://doi.org/10.1016/J.INTERMET.2022.107735.

[37] N. Yurchenko, E. Panina, A. Tojibaev, S. Zherebtsov, N. Stepanov, Overcoming the strength-ductility trade-off in refractory medium-entropy alloys via controlled B2 ordering, Mater. Res. Lett. 10 (2022) 813–823, https://doi.org/10.1080/21663831.2022.2109442.

[38] F. Liu, S. Chen, B. Wang, L. Wang, Y. Xiao, L. Wang, S. Sun, Y. Xue, High specific yield strength TiZrAlNbV high-entropy alloys via coherent nanoprecipitation strengthening, Mater. Sci. Eng. 861 (2022), 144346, https://doi.org/10.1016/j.msea.2022.144346.

[39] N. Yurchenko, E. Panina, A. Tojibaev, V. Novikov, G. Salishchev, S. Zherebtsov, N. Stepanov, Effect of B2 ordering on the tensile mechanical properties of refractory $Al^xNb_{40}Ti_{40}V_{20-x}$ medium-entropy alloys, J. Alloys Compd. 937 (2023), 168465, https://doi.org/10.1016/J.JALLCOM.2022.168465.

[40] R. Huang, W. Wang, T. Li, L. Zhang, A. Amar, X. Chen, Z. Ren, Y. Lu, A novel AlMoNbHfTi refractory high-entropy alloy with superior ductility, J. Alloys Compd. 940 (2023), 168821, https://doi.org/10.1016/j.jallcom.2023.168821.

[41] C. Zhang, H. Wang, X. Wang, Y.T. Tang, Q. Yu, C. Zhu, M. Xu, S. Zhao, R. Kou, X. Wang, B.E. MacDonald, R.C. Reed, K.S. Vecchio, P. Cao, T.J. Rupert, E. J. Lavernia, Strong and ductile refractory high-entropy alloys with super formability, Acta Mater. 245 (2023), 118602, https://doi.org/10.1016/j.actamat.2022.118602.

[42] T. Li, S. Wang, W. Fan, Y. Lu, T. Wang, T. Li, P.K. Liaw, CALPHAD-aided design for superior thermal stability and mechanical behavior in a TiZrHfNb refractory high-entropy alloy, Acta Mater. 246 (2023), 118728, https://doi.org/10.1016/j.actamat.2023.118728.

[43] Y. Jia, C. Ren, S. Wu, Y. Mu, L. Xu, Y. Jia, W. Yan, J. Yi, G. Wang, Multistage strain-hardening behavior of ultrastrong and ductile lightweight refractory complex-concentrated alloys, J. Mater. Sci. Technol. (2023), https://doi.org/10.1016/j.jmst.2022.12.011.

[44] Y. Zhang, Z. Bu, T. Yao, L. Yang, W. Li, J. Li, Novel BCC Ti-Al-Nb-Zr medium-entropy alloys with ultrahigh specific strength and ductility, J. Alloys Compd. 936 (2023), 168290, https://doi.org/10.1016/j.jallcom.2022.168290.

[45] N. Yurchenko, E. Panina, A. Tojibaev, R. Eleti, D. Volosevich, O. Klimova-Korsmik, G. Salishchev, S. Zherebtsov, N. Stepanov, Temperature-dependent plastic deformation of a refractory $Al_{7.5}(NbTiZr)_{92.5}$ medium-entropy alloy with a bcc+B2 structure, Materialia 28 (2023), 101766, https://doi.org/10.1016/j.mtla.2023.101766.

[46] G.W. Ardley, On the effect of ordering upon the strength of Cu_3Au, Acta Metall. 3 (1955) 525–532, https://doi.org/10.1016/0001-6160(55)90110-3.

[47] G. Vanderschaeve, T. Sarrazin, B. Escaig, Effect of domain size on the mechanical properties of ordered Ni_3V, Acta Metall. 27 (1979) 1251–1260, https://doi.org/10.1016/0001-6160(79)90141-X.

[48] Y. Koizumi, Y. Minamino, T. Nakano, Y. Umakoshi, Effects of antiphase domains on dislocation motion in Ti_3Al single crystals deformed by prism slip, Philos. Mag. A 88 (2008) 465–488, https://doi.org/10.1080/14786430701864746.

[49] E04 Committee, Test Methods for Determining Average Grain Size, ASTM International, n.d. https://doi.org/10.1520/E0112-10.

[50] N. Hansen, Hall–Petch relation and boundary strengthening, Scripta Mater. 51 (2004) 801–806, https://doi.org/10.1016/j.scriptamat.2004.06.002.

[51] B. Kang, J. Lee, H.J. Ryu, S.H. Hong, Ultra-high strength WNbMoTaV high-entropy alloys with fine grain structure fabricated by powder metallurgical process, Mater. Sci. Eng. 712 (2018) 616–624, https://doi.org/10.1016/j.msea.2017.12.021.

[52] B. Kang, J. Lee, H.J. Ryu, S.H. Hong, Microstructure, mechanical property and Hall-Petch relationship of a light-weight refractory $Al_{0.1}CrNbVMo$ high entropy alloy fabricated by powder metallurgical process, J. Alloys Compd. 767 (2018) 1012–1021, https://doi.org/10.1016/j.jallcom.2018.07.145.

[53] C.-H. Tu, Y.-C. Lai, S.-K. Wu, Y.-H. Lin, The effects of annealing on severely cold-rolled equiatomic HfNbTiZr high entropy alloy, Mater. Lett. 303 (2021), 130526, https://doi.org/10.1016/j.matlet.2021.130526.

[54] P.D. Littlewood, T.B. Britton, A.J. Wilkinson, Geometrically necessary dislocation density distributions in Ti–6Al–4V deformed in tension, Acta Mater. 59 (2011) 6489–6500, https://doi.org/10.1016/j.actamat.2011.07.016.

[55] A. Kundu, D.P. Field, Influence of plastic deformation heterogeneity on development of geometrically necessary dislocation density in dual phase steel, Mater. Sci. Eng. 667 (2016) 435–443, https://doi.org/10.1016/j.msea.2016.05.022.

[56] W. Gao, J. Lu, J. Zhou, L. Liu, J. Wang, Y. Zhang, Z. Zhang, Effect of grain size on deformation and fracture of Inconel718: an in-situ SEM-EBSD-DIC investigation,

Mater. Sci. Eng. 861 (2022), 144361, https://doi.org/10.1016/j.msea.2022.144361.
[57] R.Y. Umetsu, H. Ishikawa, K. Kobayashi, A. Fujita, K. Ishida, R. Kainuma, Effects of the antiferromagnetic anti-phase domain boundary on the magnetization processes in $Ni_2Mn(Ga_{0.5}Al_{0.5})$ Heusler alloy, Scripta Mater. 65 (2011) 41–44, https://doi.org/10.1016/j.scriptamat.2011.03.014.
[58] T.S. Rong, M. Aindow, I.P. Jones, The interaction between extended dislocations and antiphase domain boundaries — I: superpartial separation and the yield stress, Intermetallics 9 (2001) 499–506, https://doi.org/10.1016/S0966-9795(01)00031-0.
[59] J. Shyue, D.H. Hou, M. Aindow, H. Fraser, Deformation mechanisms in intermetallic compounds based on Nb_3Al, Mater. Sci. Eng. 170 (1993) 1–10, https://doi.org/10.1016/0921-5093(93)90363-J.
[60] T.S. Rong, D.N. Horspool, M. Aindow, Microstructure and mechanical behaviour of Nb-Al-V alloys with 10-25 at.% Al and 20-40 at.% V - II: mechanical behaviour and deformation mechanisms, Intermetallics 10 (2002) 13–21, https://doi.org/10.1016/S0966-9795(01)00077-2.
[61] D.-H. Hou, H.L. Fraser, Effect of cooling rate on the tensile yield strength and ductility of B2 compound in Nb-40at.% Ti-15at.%Al alloy, MRS Online Proc. Libr. OPL. 322 (1993) 387, https://doi.org/10.1557/PROC-322-387.
[62] S. Wang, S. Lu, M. Wu, D. Wang, G. Zhu, C. Yang, D. Shu, B. Sun, L. Vitos, Decreasing Zr content to improve tensile properties of non-equiatomic TiZrHfNb medium entropy alloys with transformation-induced plasticity, Mater. Sci. Eng. 832 (2022), 142476, https://doi.org/10.1016/j.msea.2021.142476.